

# Accuracies of Atmospheric Profiles Obtained from GPS Occultations

Kenneth R. Hardy  
Lockheed Missiles and Space Company, Inc

George A. Hajj, E. Robert Kursinski and R. Ibanez-Meier,  
California Institute of Technology  
Jet Propulsion Laboratory

## BIOGRAPHIES

*Kenneth Hardy* is a staff scientist in the Space Sciences Directorate of Lockheed Missiles & Space Co and is doing research on the use of satellites for monitoring the Earth's atmosphere and surface. Earlier he was the Chief of the Satellite Meteorology Branch of the USAF Phillips Laboratory and has twenty-five years of experience working with ground-based and satellite remote sensing systems.

*George Hajj* received his B.S. in physics from Northeastern University in 1982, and his Ph.D. in Physics from Rice University in 1988. He has worked at the Jet Propulsion Laboratory in the Earth Orbiter System group since then. His main line of work is using the Global Positioning System to do precise positioning and related applications. He is presently involved in the effort at JPL to develop the GPS occultation capability for remotely sensing the earth's atmosphere and ionosphere. He is also working on developing means of reducing ionospheric and tropospheric errors that will lead to millimeter geodesy using GPS.

*E. Robert Kursinski* is a Member of the Technical Staff of the Jet Propulsion Laboratory and is leading the JPL effort involved with developing the GPS occultation technique and applications for remotely sensing the earth's atmosphere and ionosphere. He was a member of Voyager radio science team and project manager and system engineer for the radio science system for the Voyager-2 Neptune encounter.

*Rodrigo Ibanez-Meier* received his Ph.D. in high-energy physics from Rice Univ. in 1992, and joined JPL's Tracking and Applications Section the same year. He is now working in POD and several applications of GPS/LEO systems, including Earth orientation, crustal motion, atmospheric and ionospheric observations.

## ABSTRACT

Radio occultation studies of the terrestrial atmosphere are possible through use of signals transmitted by satellites of the Global Positioning System (GPS) and received by one or more other satellites in low earth orbit (LEO). The perturbed phase of the occulted signal gives direct information on the refractivity profile in the region of

occultation, from which vertical profiles of density, pressure, and temperature can be retrieved. The technique requires the use of the dual GPS frequencies in order to isolate and remove most of the ionospheric effect. Analysis of the effect of the ionosphere and methods of removing it will be presented. For the recovery of atmospheric profiles, two major issues are addressed. The first is how accurately can reflectivity be retrieved for a region in which there is a large horizontal refractivity gradient; the second considers the separation of temperature and moisture in the lower troposphere. Based on model simulations, the capability of GPS to provide atmospheric profiles is assessed.

## 1.1 INTRODUCTION

Profiles of atmospheric refractivity can be retrieved with techniques utilizing measurements of the propagation delay of signals from Global Positioning System satellites observed by one or more receivers in low earth orbit. This is an application of the radio occultation technique originally developed in the late 1960's and early 1970's through a combination of efforts primarily at JPL and Stanford University and is well established as a technique in NASA's planetary program. The radio signal propagating from the GPS transmitter to the LEO receiver follows a path through the terrestrial atmosphere that curves in response to gradients in atmospheric refractive index. The slowing of the signal as it travels along the curved path produces an extra optical length in addition to the incremental increase in the path length.

The cumulative effect of the atmosphere on the ray path can be expressed in terms of the total refractive bending angle,  $\alpha$ , as a function of an impact parameter,  $a$ . The impact parameter is defined as the perpendicular distance between the center of the local curvature near the tangent point of the ray and the asymptotic straight line followed by the ray as it approaches the atmosphere (Fig. 1). For an atmosphere with local spherical symmetry (i.e., no horizontal variations in refractive index), there is a unique relationship between  $\alpha(a)$  and  $\mu(r)$ , the atmospheric refractive index as a function of radius  $r$ . Specifically,  $\mu(r)$  is obtained through integration of  $\alpha(a)$ , where the integral is a specific case of the Abel transform (Ref. 1), in the more general case where the contours of

constant refractivity are oblate in response to the non-spherical gravity field of a planet, the non spherical inversion can be performed (Ref 2). In the most general case, raytracing can be used in the inversion process.

The fundamental measurement in these radio occultation experiments is the Doppler shift of the received signal. When combined with a precise knowledge of the experiment geometry (obtained from concurrent observations of other GPS satellites), each sample of Doppler data can be converted to the corresponding values for  $\alpha$  and  $a$ . The refractive index profile  $\mu(r)$  is then derived from estimates of  $\alpha(a)$ .

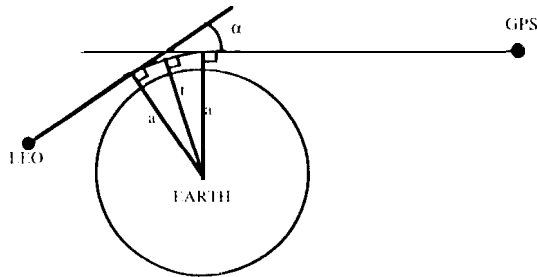


Fig 1 Occultation geometry for GPS-LEO

With a full constellation of 24 GPS satellites, a single GPS receiver in LEO, will obtain approximately 500 globally distributed profiles per day. This coverage may be sufficient for climate monitoring of stratospheric temperatures. Improvement in the spatial coverage is achieved by placing more receivers in orbit. With two receivers in low earth orbit, the number of soundings would approach that of the global radiosonde network. Because the receivers are small, of low cost and very simple devices, placing multiple receivers in orbit is a realistic possibility.

The occultation observations are unique in a number of ways. First, the principal observable is propagation delay rather than intensity as in passive sounders. For climate monitoring purposes in particular, this is important because the errors in the retrievals obtained from radio occultations will tend to be independent of those obtained from other techniques. The propagation delay can be measured very accurately and does not require any calibration parameters. The measurement precision is sub-millimeter whereas the delay caused by the atmosphere varies from a few centimeters near 60 km altitude to about 1 km at the surface.

A second unique feature is due to the signal source being essentially a point source. Therefore, the vertical and cross-beam resolution is defined approximately by the first Fresnel zone and is on the order of 1 km. Because the GPS signal frequencies (~1.5 GHz) are very low by remote sensing standards, these frequencies are well below any absorption lines of significant atmospheric constituents and the wavelengths are sufficiently long

(~20 cm) that aerosols, clouds, and rain have little effect on the propagation of the radio signal. This allows a limb sounding technique which operates down to the earth's surface. Moreover, because the signal source is observed either immediately before or after the occultation, the observations are essentially self-calibrated leading to excellent long-term stability with no associated cost of on-board calibration equipment.

The most obvious application of this technique is accurate temperature retrievals in the stratosphere. The small amount of water vapor at these altitudes has very little effect on the retrievals. A general feature of the technique which complements passive sounders is that the sensitivity generally improves with colder temperatures because the air is dry, relatively dense, and scale heights are relatively small, all of which result in a more accurate temperature retrieval (Ref 2). The occultation data also has a potential application in the area of tropospheric weather monitoring. The high vertical resolution and sensitivity to water vapor provides the potential for estimating the 10 W-ICVC1 moisture profile within the tropical marine layer (Ref 3).

A key issue is how to retrieve refractive-index profiles in a horizontally non-uniform atmosphere. The simplest retrieval technique assumes there is no horizontal variation locally to the structure, and therefore retrievals done in this manner will tend to smooth out the horizontal structure. An evaluation of the retrieval in a spatially variable atmosphere is provided in this paper. Another approach is to consider each observation as an integral measurement across the whole atmosphere, and therefore it contains information on the horizontal structure. One improvement over the spherical symmetry assumption is to combine the occultation data with nadir viewing observations from other instruments and do retrievals on the combined data set. Because the high vertical resolution of the limb-sounding geometry complements the horizontal resolution of the nadir sounders, the two techniques operating in concert may be far more powerful than either alone.

## 2. SOURCES OF REFRACTIVITY

As  $\mu$ , the index of refraction, is close to unity in the terrestrial atmosphere, it is convenient to define the refractivity  $N = (\mu - 1) \times 100$ . In the earth's atmosphere there are three main sources of refractivity affecting the passage of the GPS signals. (A fourth source is scattering from large rain drops, but it was shown in Ref 4 that this source can be neglected except under very extreme conditions.) These are referred to as dry, moist, and ionospheric terms respectively, and the approximate equation for their dependence is as follows:

$$N = 77.6 \frac{P}{T} + 3.73 \times 10^6 \frac{P_w}{T^2} - 40.3 \times 10^6 \frac{n_e}{f^2} \quad (1)$$

where

- $p$  = pressure in millibars,
- $T$  = temperature in Kelvins,
- $P_w$  = water vapor pressure in millibars,
- $n_e$  = electron number density ( $m^{-3}$ ),
- $f$  = radio frequency in Hz.

The dry term is due to the polarizability of molecules in the atmosphere, that is, the ability of an incident electric field to induce an electric field in the molecules. The moist term is due to the large permanent dipole moment of water vapor. The dry term dominates for altitudes between 0-90 km with the water vapor contribution becoming important in the lower troposphere. The ionospheric term is primarily due to free electrons in the ionosphere at altitudes higher than 90 km.

The dispersive nature of the ionosphere causes the ionospheric refractivity term to depend on the frequency (3rd term in Eq 1). This frequency dependence is exploited by the GPS dual frequencies so that the ionospheric term is isolated and removed to first order. After the removal of this term, higher order residual ionospheric terms will remain and will present a source of error in the stratosphere. This effect may be particularly important on the day side. A careful examination of residual ionospheric effects and their magnitude is provided in Section 4.

in regions where the atmosphere is dry (above 10 km altitude) only the first term on the RHS of Eq 1 is significant. Combining this with the equation of state for dry air results in

$$\rho = 0.3484 \frac{P}{T} \quad (2)$$

where  $\rho$  is the air density in  $kg\ m^{-3}$ . Comparing Eqs 1 and 2, it becomes evident that the density is directly proportional to refractivity for dry air. The pressure can then be obtained from the density by integrating the equation of hydrostatic equilibrium:

$$\frac{\partial P}{\partial h} = -g\rho \quad (3)$$

where  $h$  is height and  $g$  is the acceleration of gravity. Given  $\rho$  and  $P$ , Eq. (2) can be used to obtain  $T$ .

However, the "moist term" can be substantial in the lowest scale height of the earth's atmosphere. This term also exhibits considerable variability with location and time. The separate contributions to  $N$  by the dry and the moist terms cannot be distinguished uniquely by the occultation measurements alone. The accuracy to which these terms can be separated is a function of climatic

regime. A simple look at how well these can be separated in the two climatic regimes is presented in Ref's 3 and -1. As discussed in Ref 3, in tropical regions where the temperature structure is relatively constant, accurate estimates of water vapor profiles can be obtained using a simple average dry structure. In the other extreme, polar night, the moist contribution is so small that accurate temperature retrievals can be obtained down to the surface (Ref 4). This is consistent with the previously mentioned cold temperature retrieval capability complementing passive sensor observations. The retrieval of profiles for a non-uniform atmosphere is treated in Section 5.

### 3. ERROR SOURCES AND EXPECTED TEMPERATURE ACCURACY

Based on order of magnitude estimation, one can divide the atmosphere into several altitude and climatic regions where different error sources become significant. Below 25 km where random measurement error is a small fraction of the total refractivity, systematic errors in the assumed shape of the contours of constant refractivity are expected to dominate. Refractivity, temperature and pressure errors will grow gradually with increasing altitude until the decrease in refractivity in the thinning atmosphere causes random errors and residual ionosphere effects to dominate. Random measurement errors include short term phase instability in the clocks involved in the measurements, thermal noise in the receivers, multipath off the surroundings of the transmitters and receivers, ephemeris errors, and uncertain tropospheric delays. The dominant error sources also depend on the strategy that is being used during an occultation.

Three different approaches are possible when analyzing the occultation data. First is the no-difference technique where measurements from link A, which is the link connecting GPS1 to LEO shown in Fig 2, is used

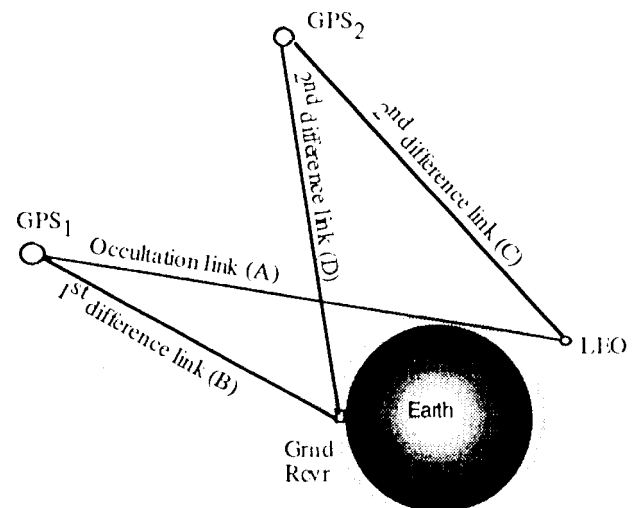


Fig 2. Single- and double-differencing geometries

alone. The second approach is the single differencing technique'. In this technique the carrier phase of link A is subtracted from that of B (link between GPS1 and a ground antenna), thereby differencing out the GPS1 clock error. The third approach is the double-differencing technique, where the following linear combination is formed:

$$(\text{link A} - \text{link B}) - (\text{link C} - \text{link D})$$

link C is between GPS2 and LEO; link D is between GPS2 and the same ground antenna, as shown in Fig 2. The double-differencing technique cancels out all clocks involved, namely those of GPS1, GPS2, LEO and the ground antenna. However, the single- and double-differencing techniques introduce new errors due to atmospheric effects induced on the signals between the GPS satellite(s) and the ground receiver. With the six existing GPS ground stations distributed evenly around the globe (such as the ones used to do orbit determination for TOPEX/POSEIDON), there is the necessary and sufficient coverage to do double differencing. Thus, for any given occultation geometry, there are always two GPS satellites that are commonly viewed by the LEO satellite and two ground stations.

Table I shows the different sources of error for the three different techniques. The symbol "x" refers to the presence of the noise source listed on the left for the particular technique. Capital **X** and bold **X** refers to the fact that the error is dominant. For instance the GPS cesium oscillator is a dominant error source of error in the no-differencing technique, while it is totally absent in the single- and double-differencing techniques. On the other hand the LEO quartz oscillator, which is about 30 times better in stability than the GPS cesium, will have an effect

in the no-differencing as well as the single-differencing technique. This error will be eliminated along with the ground hydrogen-maser clock in the double-differencing technique assuming that data are taken at the same rate from both the LEO and ground receivers. Also indicated is the type of the errors assumed and, when relevant, the time constants that are associated with these errors. The factor of (2) next to an "x" refers to the fact that the noise appears twice since it is a double differencing technique. The question mark refers to the fact that the error is not yet well understood.

Fig 3 shows the typical noise levels due to different sources. Over the 200" seconds shows, the largest error is due to the LEO quartz oscillator as seen from a ground receiver; therefore it includes the inexact specification of the troposphere. The following error sources are also shown: (1) a Hydrogen maser; (2) a LEO SNR after taking the linear combination of L1 and L2 whereby most of the ionospheric effect is subtracted out, but this linear combination increases the phase jitters by a factor of 3, (3) the ground SNR, (4) a 1 mm sine curve with a period of 300 seconds which represent the ground multipath, (5) a simulated error due to multipath off the LEO body, and (6) a velocity bias which is due to uncertainties in the LEO and GPS velocities and is taken to be 0.05 mm/sec. The error sources shown in Fig 3 do not include the residual ionospheric error, an effect which is the residual ionosphere after forming the traditional "ionospheric free" linear combination. Also not shown in the figure is the GPS cesium clock drift. A typical GPS clock error would look like that of the LEO quartz oscillator shown in Fig 3 but a factor of 30 bigger. Therefore, when an occultation link is used without differencing with any other link (no-differencing technique), then, the GPS clock oscillator is by far the most dominant error source.

TABLE I. ERROR SOURCES FOR THE THREE DIFFERENT TECHNIQUES POSSIBLE WHEN ANALYZING OCCULTATION DATA.

Noise Origin	Tau (sec)	Type	no-differencing	Single-differencing	double-differencing
Oscillators:					
GPS cesium	1	FF	<b>X</b>		
LEO quartz	1	FF	x	x	
Grnd H-maser	1	FP		x	
SNR:					
GPS to LEO	0.3	<b>WP</b>	x	x	x(2)
GPS to Grnd	0.3	<b>WP</b>		x	x(2)
Troposphere					
GPS to Grnd	1	FF		x	X(2)
Multipath:					
GPS to LEO		SIM	<b>X</b>	<b>X</b>	<b>X(2)</b>
GPS to Grnd				x	x(2)
Ionosphere:					
GPS to LEO			?	?	?
GPS to Grnd				appears in SNR	appears in SNR
GPS2 to LEO					appears in SNR

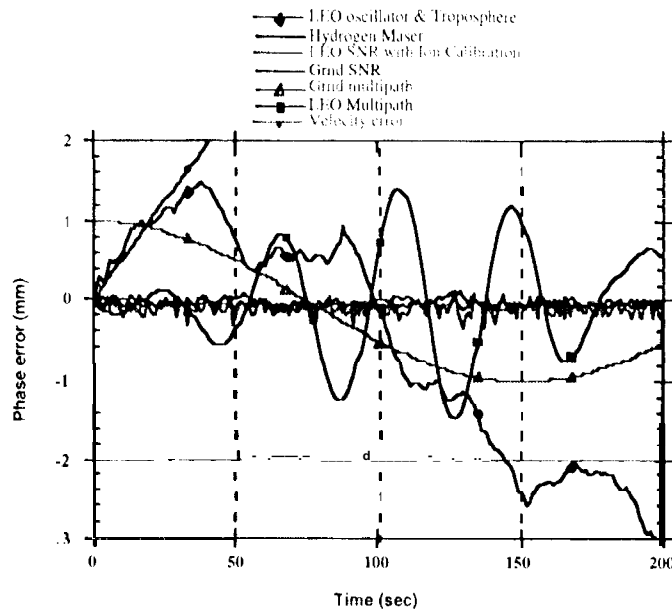


Fig 3 The estimated noise levels for seven different sources (see text for details)

in order to quantify the effect of the error-sources shown in Fig 3 on the recovery of the refractivity, pressure and temperature, the simulation procedure outlined in Fig 4 was developed. The first step is to generate atmospheric temperature and pressure profiles, and these are obtained from the US standard atmospheres included in the Handbook of (geophysics and the Space Environment published by the USAF. Ignoring water vapor, refractivity is then generated using the first term of Eq 1. Observables for a given GPS-LEO occultation geometry are generated by raytracing the signal through the assumed atmosphere. Noise is added to the simulated radio signatures which are then inverted in the manner

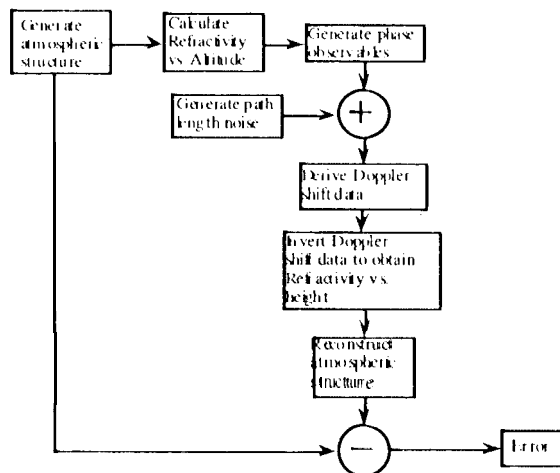


Fig 4 Procedure for simulation of some error sources that contribute to the retrieval of atmospheric profiles

described in Ref 1 to obtain the refractivity versus height. Density, pressure and temperature are obtained from the refractivity profile through the procedures described in Section 2. The resultant temperature solution is then subtracted from the initial temperature profile used in the simulation in order to obtain an estimate of the error.

Simulations were carried out using the no-differencing technique, where the dominant error is the GPS clock, as well as for the single-differencing technique which eliminates the GPS clock error. Fig 5 shows the error in the reconstructed temperature versus height for the single-differencing technique. Two different cases are plotted in Fig 5; in one case the inversion started at 69 km while in the other it started at 59 km. Each case is the RMS of four runs where the data noise shown in Fig 3 is divided into four parts, 0-50, 50-100, 100-150, 150-200 sec, and each case is run independently.

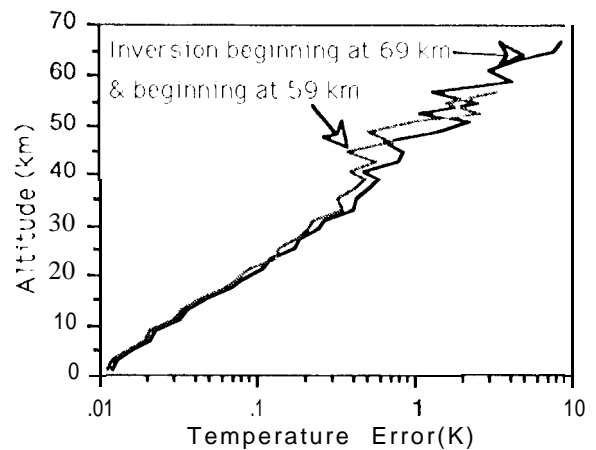


Fig 5. Temperature error due to various sources (see text for details)

Fig 5 shows that the temperature error is ~1 K at 50 km and drops to a few tenths of a degree Kelvin in the middle and lower stratosphere. Although several error sources are included in the simulations, possible significant errors due to the ionosphere as well as systematic errors due to inhomogeneity in the horizontal structure of the refractivity have been excluded. These error sources are treated separately in Sections 4 and 5. The results shown in Fig. 5 thus represent a lower bound of the temperature errors that result from random measurement errors. Moreover, the effect of water vapor has not been incorporated into the simulations results, and for most atmospheres the presence of water vapor obscures the interpretation of the refractivity below

about 7 km. The retrieval of moisture information in the lower troposphere has been described in Ref 3 and is also discussed in Section 5.

#### 4. ERRORS DUE TO THE IONOSPHERE

The earth's ionosphere which extends from about 100 km altitude upward, acts as a lens that overlays the neutral atmosphere. In an occultation geometry, the signal must pass through the ionosphere on its way into and out of the neutral atmosphere below 100 km altitude. This implies that a removal of this ionospheric effect on the signal is necessary before we can accurately deduce the neutral atmospheric profile. The dispersive nature of the ionosphere, causes the two GPS frequencies to travel at different speeds. A simple linear combination of the  $L_1$  and  $L_2$  signals can be formed to subtract out most of the ionospheric delay. This commonly used simple linear combination however, assumes that the two GPS signals are traveling along exactly the same paths. Moreover, it also ignores higher order terms in the expansion of the ionospheric index of refraction. These residual ionospheric effects, if left uncalibrated, act as an error source that maps into neutral atmospheric profile errors. In this section we will examine these ionospheric residuals in some detail.

The two GPS phase observables,  $L_1$  and  $L_2$ , can be expanded in powers of the inverse operating frequency as follows (See Appendix for details):

$$L_1 = \rho - \frac{q}{f_1^2} - \frac{1}{2} \frac{v}{f_1^3} - \frac{1}{3} \frac{r}{f_1^4} + B_1, \quad (4)$$

$$L_2 = \rho - \frac{q}{f_2^2} - \frac{1}{2} \frac{v}{f_2^3} - \frac{1}{3} \frac{r}{f_2^4} + \alpha + B_2, \quad (5)$$

where  $\rho$  corresponds to the geometrical length along the path traveled by the  $L_1$  frequency plus the delay induced by the neutral atmosphere;  $\rho$  also contains terms that are common to both  $L_1$  and  $L_2$  such as clock drifts. The coefficients  $q$ ,  $v$ , and  $r$  are factors involving integration of the electron density and magnetic field along the  $L_1$  path.  $B_1$  and  $B_2$  contain other effects such as system noise, multipath and other terms that can be solved for. The correction term  $\alpha$  is due to the fact that the two paths traveled by the  $L_1$  and  $L_2$  signals are slightly different.

The second, third and fourth terms on the right hand side of Eqs. (4) and (5) are respectively inversely proportional to the second, third and fourth power of the operating frequency. We will refer to these terms as the "first", "second" and "third" order ionospheric terms;  $\alpha$  will be referred to as the bending term. Higher-order (2<sup>nd</sup> and 3<sup>rd</sup>) and bending terms are three orders of magnitude smaller than the first-order term. In most

geodetic applications, the first order term is removed via a simple linear combination of the  $L_1$  and  $L_2$  (see Appendix, Eq. (A13)). Residual ionospheric errors are then reduced to cm level or less. These residuals, small as they are, may be a limiting error source in the neutral atmospheric reconstruction at heights above 35 km altitude. Below we estimate these residual ionospheric effects, and suggest ways of reducing them.

To proceed with the computation of the higher-order and bending terms, we have to assume models for the electron density,  $N$ , and the earth magnetic field  $B_0$ . For the electron density, we generated a 2-D grid along geomagnetic longitude using the Parameterized Ionospheric Model (PIM) (Fig. 6). This 2-D grid which extends from -80 to +80 latitude corresponds to the simulated electron density at 12:00 universal time, September 26, 1992. The density is representative of the ionosphere during the day time, and during high solar activities. PIM is a worldwide electron density profile model that is based on a parameterized version of the Utah State University model, which is a complete, first principles, ionospheric model using as inputs the solar UV flux wavelength profile, the Hedin neutral wind model, the MSIS-86 neutral atmosphere model, and an electric field model obtained from all available experimental data. The 2-D density grid has a bulge near 20 deg. north latitude. A vertical profile at that latitude is shown in figure 7. The two peaks corresponds to the F2 peak at 400 km altitude and the E peak at 100 km altitude. In our simulation, the occultation is taking place in the same longitude plane, with a tangent point at 20 deg. north latitude.

Next we need to model the earth's magnetic field. A first order approximation to the geomagnetic field near the surface of the earth is an earth-centered dipole with its

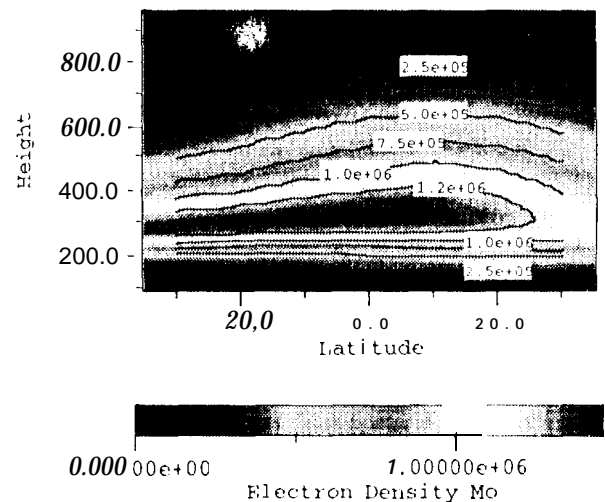


Figure 6. Electron density used to estimate higher-order and bending terms

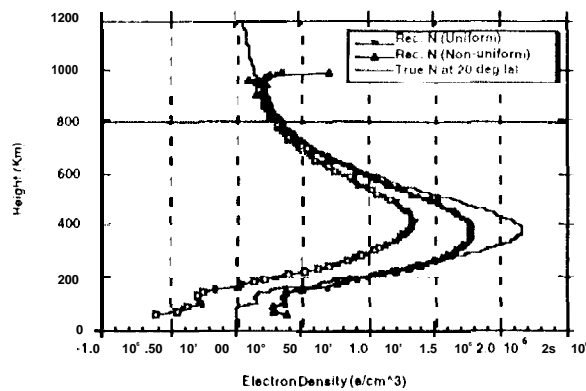


Figure 7: True and reconstructed electron density profiles at 20 deg. N latitude.

axis tilted to intersect the earth at 78.5°N latitude, 291.0°E longitude, which corresponds to the geomagnetic north pole; and at 78.5° S latitude, 111.0°E longitude which corresponds to the geomagnetic south pole (Fig. 8). In general, such an approximation is only accurate to about 75%; an approximation that is 90% accurate can be obtained by taking the dipole to be eccentric. Still a more accurate value of the magnetic field can be obtained by using the International Geomagnetic Reference Fields; however, our aim is to get a first order assessment of the higher-order and bending terms. These terms are small, but can be limiting sources of error in the temperature profile retrieval in the upper stratospheric heights. The complexity of the models used to estimate these errors need only to be consistent with the required accuracies.

Based on these models, we estimate the residual ionospheric terms after forming the traditional "ionospheric free" linear combination (Eq. (A13) of Appendix) Figure 9 shows the residuals due to the

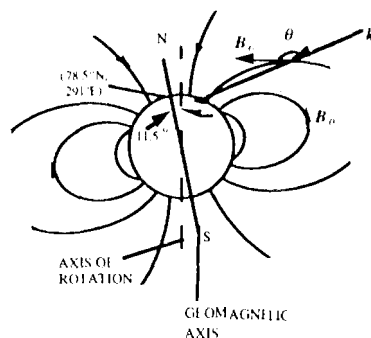


Figure 8: The earth's magnetic field modeled as an earth centered dipole, aligned along the geomagnetic axis.

second- and third-order terms as well as bending versus the height of the tangent point of the occultation link. It is clear from the figure that the dominant error is due to bending. This error becomes particularly large at heights near 100 km altitude corresponding to the bottom of the E layer. The maximum bending error at 100 km corresponds to the time when the ray is experiencing the sharp vertical gradient of the index of refraction in the tail of the E layer.

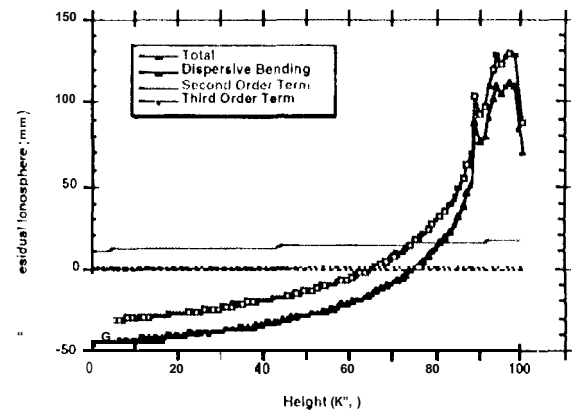


Figure 9: Residual ionospheric error after forming the traditional "ionospheric free" linear combination.

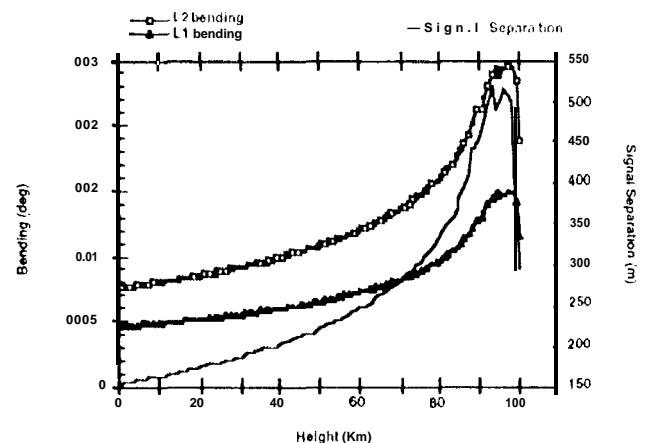


Figure 10: Bending of the L1 and L2 signals and the separation distance between the nearest approach points of the two signals.

The effect of the dispersive bending is understood further as we examine the amount of bending experienced by each signal as shown in figure 10. The L1 and L2 signals experience a maximum bending of 0.02 and 0.03 degrees respectively. The positive bending implies that the signals are curved away from the earth. This curvature

changes sign when the tangent point is at altitudes higher than the F2 region. Also shown in the figure is the separation distance between the two tangent heights of the  $L_1$  and  $L_2$  raypaths. The separation distance ranges between  $\sim 150$  m near the surface of the earth to about 500 m at 100 km altitude.

On the other hand, typical night time ionosphere residuals are less than 1 mm up to 80 km altitude which is below some of the noise levels considered in the previous section (see Fig. 3). This implies that generally speaking the night time ionosphere does not represent a problem to neutral atmospheric temperature recovery. In contrast, the day time ionospheric residual error ranges from -3 to +3 cm between heights of 20-80 km, which would create a serious error in the recovered temperature in the upper part of the stratosphere. This phase change of 6 cm corresponds to 0.5 % of the total atmospheric delay experienced at 20 km.

We are pursuing methods of further reducing this error which utilize information on the vertical structure of the ionosphere recovered by inverting the ionospheric occultation data. An example of the solution thus obtained under the assumption of local spherical homogeneity is shown in Fig. 6 (labeled "Uniform"). A better reconstruction is obtained when a horizontal gradient in the electron density was assumed (labeled "Non-uniform" in Fig. 6). This horizontal gradient is obtained from ground zenith TEC measurements and distributed equally across all the ionospheric layers. It is important to notice that the point-to-point structure of the E-layer is recovered in the profile, the absolute level of the density however is off. This can be improved by applying the constraint that the electron density must fall off to zero near 90 km, and not exceed a certain limit within the E region. This will be investigated further in subsequent studies.

## 5. NEUTRAL ATMOSPHERIC PROFILES

We have taken a first order look at two of the major issues concerning the accuracy and applications of occultation observations of the GPS in the neutral atmosphere (troposphere, stratosphere, and mesosphere). The first issue is how accurately can refractivity be retrieved given the relatively large horizontal variations in the refractivity structure that sometimes occurs. The second issue is related to tropospheric water vapor and concerns how well can the moist and dry terms be separated from the refractivity estimates.

As seen from Eqs 1-3, once the ionospheric term has been removed, the temperature can be retrieved in regions where moisture is negligible. For the earth's atmosphere, moisture has little effect on the refractive index when the temperature is less than about 245 K. Thus, for occultation measurements from the GPS, temperatures can be retrieved from about 60 km down to about 7 km. For the special case of polar profiles in winter, water vapor densities are sufficiently small that

very profiles of temperature can be retrieved down to the surface (Ref 4). In the tropical regions over the oceans, the temperature profiles tend to be rather uniform. Making use of this information allows the moisture profile in the lower few kilometers of the atmosphere to be accurately retrieved (Ref 3).

For occultation measurements using GPS, the radio path traverses about 2,000 km of the atmosphere for the ray which is tangent to the earth's surface. The previously mentioned results in Refs 3 and 4 assume a horizontally uniform atmosphere over this 2,000 km. Under these conditions, the Abel transform provides a very accurate reconstruction of the refractive index profile. However, the earth's atmosphere often has considerable structure in the horizontal dimension. The effect of variable horizontal structure was briefly discussed in Ref 4 where the reader is referred to gain background on how this structure affects the retrieval process. Here, in an attempt to estimate the upper limit of the impact of horizontal structure of the atmosphere on the retrieval of profiles from GPS data, we have simulated an occultation through the center of a strong frontal surface. We believe this represents extreme behavior first because it is extreme weather behavior but also because the occultation raypaths are orthogonal to the front line and because the tangent points of the raypaths fall right in the average center of the front (distance = 1,000 km in Fig 8). It should be understood that if the raypaths were parallel to the front, then the horizontal variations would be much smaller and retrievals would be very accurate.

The temperature structure for the cross section is shown in Fig 8; it was adapted from a cross section presented in Ref 8. Only data up to a height of 14 km is shown in Fig 8, but for the occultation simulations, both temperature and moisture information from the surface up to a height of 70 km was generated. The cross section shows the strong front extending from the surface at about 1,500 km up to a height of about 12 km at a distance of 700 km. The change across the 2,000 km of the cross-section is representative of a very pronounced front that might be found at mid latitudes over continents during the winter. The structure in the cross-section of the stratosphere and the mesosphere also contains features that are consistent with those expected between a very cold air mass and a warm air mass.

The refractive index was computed from the temperature and moisture cross-sections. The change in the refractivity from one end of the cross-section to the other ranged from about 50 % at 70 km to about 10 % near the surface. Typical variability of the refractivity within the troposphere of the cross-section was about 15%.

Using this weather front structure, the accuracy of tropospheric refractivity retrievals under somewhat extreme conditions can be assessed. Applying the simulation system described in Section 3, signal paths



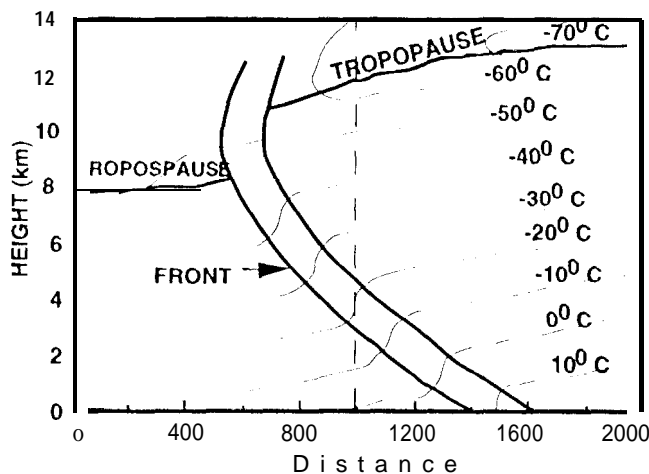


Fig 8 Vertical cross-section of temperature for a strong frontal surface

from the GPS satellite to a receiver in LEO were traced through the weather front shown in Fig 8 to generate a simulated data set. This was inverted to recover the apparent vertical refractivity structure at the center of the cross-section at 1,000 km under the assumption of local spherical symmetry (the Abel transform solution), if the atmospheric structure for the cross-section exhibits only a linear change, the Abel transform still provides an excellent solution for the center profile. The reason is that an excess contribution of the refractive index to the observed phase change from one side of the center will be offset by a corresponding deficiency on the other side of the center. On the other hand, refractive-index structure that is symmetric about the center profile, such as either a relative minimum or maximum value at the center, will introduce errors when the Abel transform solution is used (Ref 4). Thus the retrievals provide an initial estimate of the effect of symmetric atmospheric structure relative to the center (at 1000 km). The results are shown in Fig 9. Except at the very highest levels and near the surface, the errors can be expected to be less than 1%, and for many heights the error is less than 0.6% even with the local spherical symmetry assumption. The Abel transform solution is convenient to provide initial estimates of the effect of a non-uniform atmosphere on the retrieval of the refractive-index profiles. However, other techniques have already been developed to handle a non-uniform atmosphere (Ref 2), and when these are applied, it is expected that the errors in the recovery of refractive index will generally be smaller than those shown in Fig 9.

Once the ionosphere contribution to the refractive index is removed, the procedure outlined in Section 2 provides the steps to retrieve the temperature at the center of the cross-section shown in Fig 8. The pressure profile is computed by integrating the refractive index profile beginning at the top of the profile or 70 km in our example. The integration can proceed down to a height where moisture starts contributing to the refractive index

which in the profile of Fig 8 is about 8 km. In order for the integration to proceed to the surface, an average lapse rate in temperature of  $6\text{ K km}^{-1}$  was assumed from 8 km to the surface; this step leads to an estimate of the first term of Eq 1 and by subtracting this estimate from the simulated refractive index, information on the moisture profile is obtained.

The results of this retrieval procedure are shown in Fig 10. Since the pressure at the top of the profile would, in general, not be known, an error of 5% in the pressure at a height of 70 km was introduced. The effect of the unknown pressure at the start of the integration is largely removed after descending about two scale heights to near 60 km. For much of the stratosphere, the error in the temperature is less than 0.5 K. The variable structure in the cross-section near the tropopause leads to an increased error in the temperature profile at heights between 9 and 12 km. Below 8 km, the error is a reflection of how well

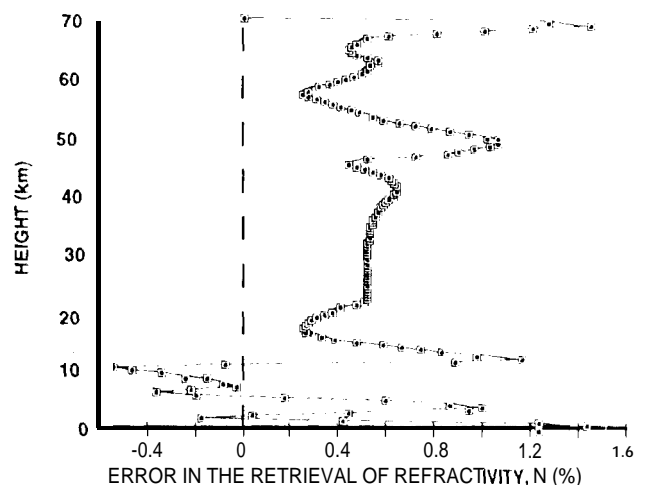


Fig 9 Error in the retrieval of refractive index at the center of the cross section shown in Fig 8

the assumed average lapse rate matches the actual profile. The large errors in the temperature estimates in this altitude region also cause large errors in the water vapor estimates. As shown in Ref 3, the retrieval of moisture in the lowest 5 km of the troposphere depends very strongly on how well the temperature can be estimated independent of the occultation observations. These results in the lower troposphere should be viewed as upper limits in that they do not take advantage of additional information on the temperature and pressure structure provided from other sensors and weather models which will improve these results. Combining these observations with these other sources of information needs further research.

The situation of the front is in marked contrast to the situation encountered with marine boundary layer inversions where the refractive-index profile is useful for identifying the height of the inversion because both

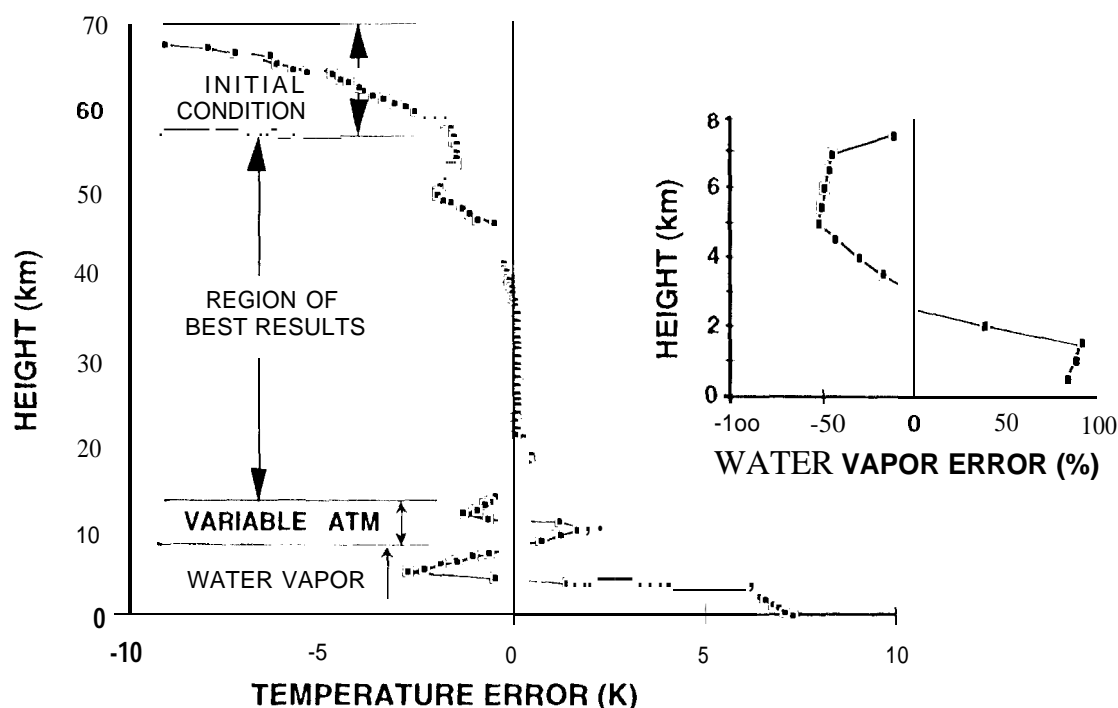


Fig 10 The error in the retrieval of temperature or water vapor for at the center of the cross-section shown in Fig 8

temperature and moisture contribute to the existence of a very strong refractivity gradient at the top of the boundary layer (Ref. 3). Unfortunately, in the case of a front, the moist and dry effects tend to cancel. On the front's cold side, the air is denser but contains less water so the dry contribution is larger and the moist term is smaller than the relative contributions of their counterparts on the warm side with the net result that remarkably little microwave refractivity contrast exists across the front. Therefore, for the case of a highly variable atmosphere in the mid latitudes, the optimum use of the occultation measurements may be in using the refractive-index profile as a limit for contributions by both temperature and moisture.

## 6. CONCLUSIONS

Some insight into the mechanism of the radio occultation technique and its potential performance in the presence of ionospheric effects and noise sources on GPS occultation measurements has been described. The effects of horizontal structure associated with a weather front on the retrieval of refractive index, temperature, and moisture have also been presented. Treating the horizontal issue is particularly important because it may be the largest error source in the troposphere. Even with large horizontal changes in the atmosphere, temperatures in the stratosphere and upper troposphere may be retrieved with an error of less than 1 K.

## ACKNOWLEDGMENTS

Some of the work described in this paper was carried out in part by the Jet Propulsion Laboratory, California Institute of Technology, under contract with the National Aeronautics and Space Administration.

## APPENDIX

### EFFECT OF THE IONOSPHERE ON THE GPS SIGNALS

The index of refraction for the ionosphere,  $n$ , is given by the Appleton-Hartree formula

$$n^2 = 1 - \frac{2X(1-X)}{2(1-X) - Y_T^2 \pm \sqrt{Y_T^4 + 4(1-X)^2 Y_L^2}}, \quad (\text{A1})$$

where

$$X = \left( \frac{f_p}{f} \right)^2 = \frac{(N e^2 / 4 \pi^2 \epsilon_0 m)}{f^2}, \quad (\text{A2})$$

$$Y_T = Y \sin \theta_R; Y_L = Y \cos \theta_R, \quad (\text{A3})$$

$$Y = \frac{f_s}{f} = \frac{(e/4\pi m)}{f} \quad (A4)$$

$N$  is the number density of electrons,  $e$  and  $m$  are the electron charge and mass, respectively,  $\epsilon_0$  is the permittivity of the free space,  $f_p$ ,  $f_g$  and  $f$  are the plasma-, gyro- and carrier frequencies respectively,  $\theta_B$  is the angle between the earth's magnetic field  $B_0$  and the direction of propagation of the wavefront  $k$ ,  $B_0$  is the magnitude of  $B_0$ . By definition  $Y = eB_0/2\pi m$ , and since for electrons  $e$  is negative,  $Y$  is antiparallel to  $B_0$ . For the earth's ionosphere, with  $N = 10^{12}$  electrons/m<sup>3</sup> the plasma-frequency  $f_p \approx 8.9$  MHz. The gyro-frequency for an electron in earth's magnetic field ( $2 \times 10^{-5}$  Tesla) is  $f_g \approx .59$  MHz.

The plus and minus signs of Eq. (1) correspond to the ordinary and extraordinary wave modes of propagation respectively. When the carrier frequency is large compared to plasma- and gyro-frequencies, as is the case with the GPS frequencies, the principal modes of propagation are dominantly circularly polarized. Ignoring the LCP component of the GPS signal which has less than .35% and 2.5% of the total power, for L1 and L2 respectively, only the (-) sign will be of relevance to us in the subsequent analysis,

in powers of the inverse carrier frequency, the index of refraction for the ionosphere can be written as

$$n = 1 - \frac{1}{2} X - \frac{1}{2} XY \cos \theta_B + \frac{1}{4} X^2 + \frac{1}{2} X + Y^2 (1 + \cos^2 \theta_B) \quad (A5)$$

The phase delay of a signal passing through the ionosphere is given by

$$\tau = \frac{1}{c} \int_{curve} n ds, \quad (A6)$$

where  $ds$  is an element of length along the curved path that the signal travels (see Fig. A1), and  $c$  is the velocity of light in vacuum. The integral for L1 and L2 is along the curved path that each signal travels. Using Eqs. (A2)-(A6) the GPS carrier phase observable can be written, in the dimension of length, as

$$L_1 = \rho - \frac{q}{f_1^2} - \frac{1}{2} \frac{v}{f_1^3} - \frac{1}{3} \frac{r}{f_1^4} + B_1, \quad (A7)$$

$$L_2 = \rho - \frac{q}{f_2^2} - \frac{1}{2} \frac{v}{f_2^3} - \frac{1}{3} \frac{r}{f_2^4} + \alpha + B_2, \quad (A8)$$

where

$$q = \frac{1}{2} \int_{curve} f_p^2 ds = (-103) \int_{curve} N dL = 40.3 TEC, \quad (A9)$$

$$v = \int_{curve} f_g f_p^2 |\cos \theta_B| ds = 7527 c \int_{curve} NB_0 |\cos \theta_B| ds, \quad (A10)$$

$$r = (2437) \int_{curve} N^2 ds + 4.74 \times 10^2 \int_{curve} NB_0^2 (1 + \cos^2 \theta_B) ds. \quad (A11)$$

$$\alpha = -\frac{1}{2} \int_0^S \frac{1}{X^2} \left( \int_0^X \left[ \frac{1}{\rho} + \frac{\partial n}{\partial z} \right] X' dX' \right)^2 dX \quad (A12)$$

$TEC$  is the total electron content along the path of integration,  $\lambda$  is the operating wavelength. In Eqs. (A7) and (A8),  $\rho$  corresponds to the geometrical distance plus the neutral atmospheric delay along the path traveled by the L1 signal. It also contains all the non-dispersive terms that are common to both frequencies such as clocks, transmitter and receiver delays. In Eq. (A7) and (A8)  $B_1$  and  $B_2$  are the sum of constant biases, multipath, system noise, phase center variations and a transmitter/receiver relative geometry dependent term. Some of these terms, such as multipath and system noise, have already been considered earlier. The other terms can be solved for.

The second, third, and fourth terms on the right-hand side of Eq. (A7) and (A8) are proportional to the inverse-square, inverse-cube, and inverse-quartic powers of frequency, respectively. The term,  $\alpha$ , is a curvature correction term. The dispersive ionosphere causes the two signals to travel along two different paths (Fig. A1). It should be noted that when computing the observables  $L_1$

and  $L_2$  based on Eq. (A6), we integrated along the same path, namely that of  $L_1$ . The term,  $\alpha$ , is to correct for the difference of integration between path  $L_1$  and  $L_2$ . This difference is computed by Williams [Ref. 9] and Gu et. al. [Ref. 10] and is given by Eq. (A 12) for propagation in a plane. The integration in Eq. (A 12) is along the straight line connecting the transmitter and the receiver,  $\rho$  is the curvature of the  $L_1$  path,  $n$  is the index of refraction and  $z$  is the direction normal to  $X$  (Fig. A1).

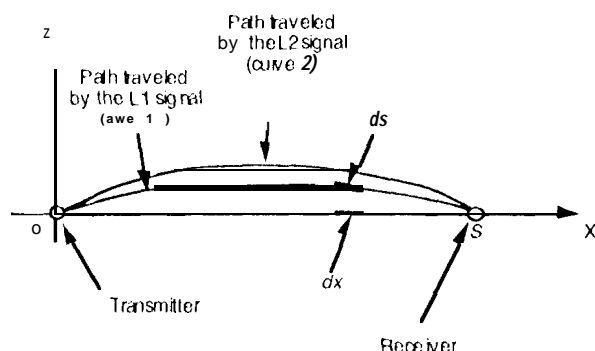


Figure A1: Pictorial representation of the path traveled by the GPS L1 and L2 signals.

The following linear combination removes the first-order ionospheric term

$$\left( \frac{f_1^2}{f_1^2 - f_2^2} \right) L_1 - \left( \frac{f_2^2}{f_1^2 - f_2^2} \right) L_2 = \rho - \frac{v}{f_1 f_2 (f_2 + f_1)} - \frac{r}{f_1^2 f_2^2} - \left( \frac{f_2^2}{f_1^2 - f_2^2} \right) \alpha \quad \text{A1.2}$$

## REFERENCES

- [1] G. Fjeldbo, A. J. Kliore, and V. R. Eshleman, "The neutral atmosphere of Venus as studied with the Mariner V radio occultation experiments", *Astronom. J.*, vol. 76, No. 2, pp. 123-140, March 1971.
- [2] G. F. Lindal, "The atmosphere of Neptune: an analysis of radio occultation data acquired with Voyager 2", *Astronom. J.*, vol. 103, pp. 967-982, March 1991.
- [3] E. R. Kursinski, G. A. Hajj and K. R. Hardy, "Temperature or moisture profiles from radio occultation measurements", *Proceedings of the Eighth Symposium on Meteorological Observations and Instrumentation*, pp. J153-J158, Amer. Meteorol Soc., Anaheim CA, January 17-22, 1993.
- [4] E. R. Kursinski, G. A. Hajj and K. R. Hardy, "Atmospheric profiles from radio occultation measurements of GPS satellites", *Proc of Conf 1995 Internat Soc for Optical Eng*, Orlando FL, May 1993.

- [5] F. J. Rich and Su. Basu, "Ionospheric Physics", *Chap 9 of Handbook of Geophysics and the Space Environment*, Ed A. S. Jursa, Air Force Geophy Lab, 1985.
- [6] H. Rishbeth and O. K. Garriott, "Introduction to Ionospheric Physics", *Academic Press*, 1969.
- [7] D. J. Knecht and B. M. Shuman, "The Geomagnetic Field" *Chap 4 of Handbook of Geophysics and the Space Environment*, Ed A. S. Jursa, Air Force Geophy Lab, 1985.
- [8] E. Palmén and C. W. Newton, "Atmospheric Circulation Systems", *Academic Press*, New York.
- [9] Williams D. C. (1975) "A theory of the curvature correction in electromagnetic distance measurement," *Survey Review*, Vol. 23, pp. 100-172.
- [10] Gu M. and Brunner F. K. (1990) "Theory of the two frequency dispersive range collection," *manuscripta geodastica*, Vol. 15, pp. 357-361.

Ionospheric expansion term	$\lambda$ (MKS units)	<u>L1</u>	<u>L2</u>	<u>(RRE)<sub>g</sub></u>
<b>1<sup>st</sup> order:</b> $1/f^2$ term:	$4.48 \times 10^{16} A^2 \text{TEC}$	16.2 m	26.7 m	0.0
<b>2<sup>nd</sup> order:</b> $1/f^3$ term:	$\approx a \cdot 2.61 \times 10^{18} A^3 \text{TEC}$ ( $0 < a < 2$ )	$\sim 1.6$ cm	$\sim 3.3$ cm	$\sim -1.1$ cm
<b>3<sup>rd</sup> order:</b> $1/f^4$ term: ( $N_{\text{max}} = 3.0 \times 10^{12} \text{ e/m}^2$ )	$\sim 2.0 \times 10^{-31} \lambda^4 N_{\text{max}} \text{TEC}$	-0.86 mm	-2.4 mm	$\sim -0.66$ mm
calibrated $1/f^3$ term based on a thin layer ionospheric model:				-1-2 mm

Table 1: Estimated zenith ionospheric group delay due to  $1/f^2$ ,  $1/f^3$  and  $1/f^4$  terms, for an arbitrary wavelength  $\lambda$  (microwave region), L1 and L2 frequencies as well as the residual range error obtained from group delay measurements with dual-frequency calibration. It is assumed that the zenith TEC  $\approx 10^{18} \text{ (e/m}^2\text{)}$ . The phase advance can be read from this

## 5. Conclusion

We summarize our results in table 1, which shows the amount of group delay due to 1<sup>st</sup>, 2<sup>nd</sup> and 3<sup>rd</sup> ionospheric terms in the zenith direction, assuming a zenith  $TEC = 10^{18}$  (e/m<sup>2</sup>).

In employing a Chapman distribution and a dipole approximation for the magnetic field, we were able to estimate the higher-order ionospheric effects on range and phase measurements. The second-order error can be several centimeters for range as well as phase during daytime, for a year near sunspot maximum. Moreover, since the magnetic field is fixed to the earth, and the GPS orbit, as seen from a ground station, repeats itself daily (shifted by  $\sim 4$  min. per day), the diurnal shape of the second-order error is most likely to repeat its overall structure for several days, at least to the extent that the overall electron density distribution remains unchanged. Such daily repeatable error in range and phase will be mapped directly into orbital and baselines estimation. Our study shows that a rough ionospheric model consisting of a thin shell at 300 km, plus a knowledge of the  $TEC$ , allows us to calibrate the second-order term to better than 90%. This implies reducing the second-order ionospheric error to less than 2 mm on the average and, therefore, potentially improving orbit determination and baseline solutions.

## Acknowledgment

We wish to thank Sien Wu and Thomas Yunck of JPL for helpful comments and suggestions on this paper. This work was performed at the Jet Propulsion Laboratory, California Institute of Technology, under contract with the National Aeronautics and Space Administration.

## References

- Bassiri S. (1990) Three frequency ranging systems and their applications to ionospheric studies. Telecommunications and Data Acquisition Progress Report 42-103, pp. 14-20, Jet Propulsion Laboratory, Pasadena, California, July -Sep.
- Bertiger WI, Wu JT, Wu SC (1992) Gravity field improvement using GPS data from Topex/Poseidon: a covariance anal ysis. *J. Geophys. Res.*, 97:1965-1971.
- Brunner FK, GU M (1991) An improved model for the dual frequency ionospheric correction of GPS observations. Manuscript *Geodaetica*, Vol. 16.
- Budden KG (1985) The propagation of radio waves, Cambridge University Press, Cambridge.
- Coco D (1991) GPS - Satellites of opportunity for ionospheric monitoring. *GPS World*, October, pp. 47-50.
- Davis K (1 966) Ionospheric radio Propagation, Dover, New York.
- Freedman AP (1991) Measuring earth orientation with global positioning system. *Bull. Geod.*, 65:53-65.
- Freymueller JT, Kellogg JN (1990) The extended tracking network and indications of baseline precision and accuracy in the North Andes, *Geophys. Res. Let.*, 17:207-210.

- Gu M, Brunner FK** (1990) Theory of the two frequency dispersive range correction. Manuscript *Geodaetica*,15:357-361.
- Hartmann GK, Leiting R** (1984), Range errors due to ionospheric and tropospheric effects for signal frequencies above 100 MHz. *Bull. Geod.*, 58:109-136.
- Jursa AS** (cd) (1985) Handbook of Geophysics and the space environment, Air Force **Geophysics** Laboratory, Bedford, Mass.
- Kellogg JN, Dixon TH (1990) Central and South America GPS geodesy- CASA UNO, *Geophys. Res. Let.*, 17:195-198.
- Lichten SM** (Apr. 1990) Estimation and filtering for high-precision GPS positioning application. Manuscript *Geodaetica*,15:159-179.
- Lichten SM** (Feb. 1990) Precise estimation of tropospheric path delays with GPS techniques. NASA TDA Progress 'Report, 42-100:1-12.
- Lichten SM** (Mar. 1990) Toward GPS orbit accuracy of tens of centimeters. **Geophys. Res. Let.**,17:215-218.
- Lichten SM, Border JS** (1992) Strategies for high precision global positioning system orbit determination. *J. Geoph. Res.*, 92:12751-12762.
- Malla RP, Wu SC** (1989) GPS inferred geocentric reference frame for satellite positioning and navigation. *Bull. Geod.*,63:263-279
- Papas CH** (1965) Theory of Electromagnetic Wave Propagation, McGraw-Hill, New York.
- Rishbeth H, Garriott OK** (1969) Introduction to ionospheric physics. Academic Press, New York.
- Spilker JJ** (1978) GPS signal structure and performance characteristics, *Navigation*, 25:29-54.
- Thornton CL, Fanselow JL, Renzetti NA** (1986) **GPS-based** geodetic measurement systems In: Anderson A, Cazenave A (eds), *Space Geodesy and Geodynamics*. Academic Press.
- Wu SC, Yunck TP, Thornton CL** (1991) Reduced dynamic technique for precise orbit determination of low earth satellites, *J. Guidance, Control and Dynamics* 14:24-30.
- Yunck TP, Wu SC, Wu JT** (1987') Precise near-earth navigation with GPS: A survey of techniques, NASA TDA Progress Report 42-91:29-45.
- Yunck TP, Melbourne WG, Thornton CL** (1985) **GPS-based** satellite tracking system for precise positioning. *IEEE Tr. Geosci. and Rem. Sensing*, GE-23, pp 450-457.